


 Single-Molecule Magnets **Hot Paper**

 How to cite: *Angew. Chem. Int. Ed.* **2024**, *63*, e202317678
 doi.org/10.1002/anie.202317678

Bimetallic Synergy Enables Silole Insertion into THF and the Synthesis of Erbium Single-Molecule Magnets

Siddhartha De, Arpan Mondal, Sean R. Giblin, and Richard A. Layfield*

Abstract: The potassium silole $K_2[SiC_4-2,5-(SiMe_3)_2-3,4-Ph_2]$ reacts with $[M(\eta^8-COT)(THF)_4][BPh_4]$ ($M = Er, Y$; COT = cyclo-octatetraenyl) in THF to give products that feature unprecedented insertion of the nucleophilic silicon centre into a carbon-oxygen bond of THF. The structure of the major product, $[(\mu-\eta^8:\eta^8-COT)M(\mu-L^1)K]_\infty$ ($\mathbf{1}_M$), consists of polymeric chains of sandwich complexes, where the spiro-bicyclic silapyran ligand $[C_4H_8OSiC_4(SiMe_3)_2Ph_2]^{2-}$ (L^1) coordinates to potassium via the oxygen. The minor product $[(\mu-\eta^8:\eta^8-COT)M(\mu-L^1)K(THF)]_2$ ($\mathbf{2}_M$) features coordination of the silapyran to the rare-earth metal. In forming $\mathbf{1}_M$ and $\mathbf{2}_M$, silole insertion into THF only occurs in the presence of potassium and the rare-earth metal, highlighting the importance of bimetallic synergy. The lower nucleophilicity of germanium(II) leads to contrasting reactivity of the potassium germole $K_2[GeC_4-2,5-(SiMe_3)_2-3,4-Me_2]$ towards $[M(\eta^8-COT)(THF)_4][BPh_4]$, with intact transfer of the germole occurring to give the coordination polymers $[\{\eta^5-GeC_4(SiMe_3)_2Me_2\}M(\eta^8-COT)K]_\infty$ ($\mathbf{3}_M$). Despite the differences in reactivity induced by the group 14 heteroatom, the single-molecule magnet properties of $\mathbf{1}_{Er}$, $\mathbf{2}_{Er}$ and $\mathbf{3}_{Er}$ are similar, with thermally activated relaxation occurring via the first-excited Kramers doublet, subject to effective energy barriers of 122, 80 and 91 cm^{-1} , respectively. Compound $\mathbf{1}_{Er}$ is also analysed by high-frequency dynamic magnetic susceptibility measurements up to 10^6 Hz.

relaxation sparked a proliferation in the development of single-molecule magnets (SMMs) during the last two decades.^[1–3] Beyond fundamental interest in the physics of SMMs, this type of molecular magnet has also shown potential for applications in nanoscale devices and quantum technologies.^[4,5] Understanding the complex magnetic relaxation phenomena shown by SMMs has been a major challenge in the development of the field, with significant progress being achieved using sophisticated theoretical models.^[6–10] Application of these models has allowed synthetic approaches to lanthanide SMMs to reach a level where chemical control of the properties is becoming possible. Notable methodologies include symmetry-based designs to increase the effective energy barrier to reversal of the magnetization (U_{eff}),^[11–14] the use of radical ligands^[15–17] and encapsulation of lanthanides in fullerenes to improve the hysteresis properties and the blocking temperature (T_B).^[18–20]

Arguably, the most successful general approach to SMM synthesis has focused on pseudo-two-coordinate dysprosium metallocene cations, $[Dy(\eta^5-Cp^R)_2]^+$, where Cp^R is a bulky cyclopentadienyl ligand such as $C_5^tPr_5$ or $1,2,4-C_5^tBu_3H_2$.^[21–27] Advances with dysprosium SMMs have also stimulated interest in isolobal replacement of cyclopentadienyl ligands with analogues containing heteroatoms such as boron,^[28] germanium,^[29] lead^[30] and phosphorus.^[31,32] Significant findings include the borolide-ligated SMM $[\{\eta^5-1-(piperidino)-2,3,4,5-BC_4Ph_4\}_2Dy]^-$,^[33] in which the dianionic ligands are thought to induce very strong crystal field splitting at the Dy^{3+} centre, leading to a U_{eff} of 1600 cm^{-1} .

The use of main group heterocyclopentadienyl ligands in lanthanide chemistry also offers the intrigue of new chemical bonding environments, including metal-heteroatom interactions with potential to lead to new reactivity. Silicon as a donor atom is notable by its absence from the family of heteroatom-containing lanthanide metallocene SMMs. Indeed, rare-earth complexes of dianionic silole ligands $[SiC_4R_4]^{2-}$ ($R = \text{alkyl, aryl, silyl}$) are limited to a single example containing lanthanum,^[34] and even in transition metal chemistry the silole ligand is rare.^[35–38] This gap in knowledge motivated us to target the silole-ligated erbium SMM $[\{\eta^5-SiC_4(SiMe_3)_2Ph_2\}Er(\eta^8-COT)]^-$, (COT = cyclo-octatetraenyl) containing the dianionic silole ligand $[SiC_4-2,5-(SiMe_3)_2-3,4-Ph_2]^{2-}$ (Cp^{Si}), the synthesis of which was reported previously by Müller et al.^[39] For comparative purposes, we also targeted the germole-ligated sandwich complex $[\{\eta^5-GeC_4(SiMe_3)_2Me_2\}Er(\eta^8-COT)]^-$, containing $[GeC_4-2,5-(SiMe_3)_2-3,4-Me_2]^{2-}$ (Cp^{Ge}),^[39] to establish whether the group 14 heteroatom impacts on the SMM properties.

Introduction

The landmark discovery that some terbium and dysprosium complexes containing one metal ion display slow magnetic

* Dr. S. De, Dr. A. Mondal, Prof. R. A. Layfield
 Department of Chemistry, School of Life Sciences
 University of Sussex
 BN1 9RH Brighton, U.K.
 E-mail: r.layfield@sussex.ac.uk

Prof. S. R. Giblin
 School of Physics and Astronomy, Cardiff University
 CF24 3AA Cardiff, UK

© 2024 The Authors. Angewandte Chemie International Edition published by Wiley-VCH GmbH. This is an open access article under the terms of the Creative Commons Attribution License, which permits use, distribution and reproduction in any medium, provided the original work is properly cited.

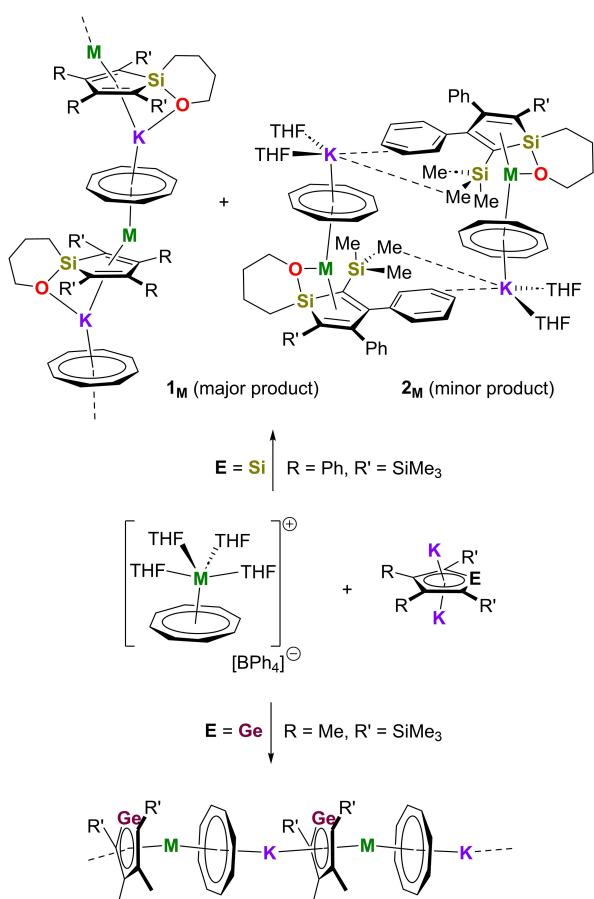
Whereas the synthesis of the germole-ligated sandwich complex proceeded as expected, divergent reactivity was observed with the silicon chemistry, resulting in an unprecedented insertion of the silole ligand into THF.

Results and Discussion

Refluxing $[\text{K}_2\text{Cp}^{\text{Si}}]$ and $[\text{Er}(\eta^8\text{-COT})(\text{THF})_4][\text{BPh}_4]$ in THF/toluene overnight produced, after work-up, yellow crystals of the heterobimetallic coordination polymer $[(\mu\text{-}\eta^8\text{:}\eta^8\text{-COT})\text{Er}(\mu\text{-L}^1)\text{K}]_\infty$ ($\mathbf{1}_{\text{Er}}$) (Scheme 1), where L^1 is the spiro-bicyclic silapyran ligand $[\text{C}_4\text{H}_8\text{OSiC}_4(\text{SiMe}_3)_2\text{Ph}_2]^{2-}$, generated by insertion of the silole silicon atom into a C–O bond of THF. The yield of $\mathbf{1}_{\text{Er}}$ was 68%. Storing the nascent solution for a further seven days gave a second, dimeric product $[(\mu\text{-}\eta^8\text{:}\eta^8\text{-COT})\text{Er}(\mu\text{-L}^1)\text{K}(\text{THF})_2]_2$, which also contains L^1 ($\mathbf{2}_{\text{Er}}$), in 5.5% yield. By reducing the reaction time to two hours, $\mathbf{1}_{\text{Er}}$ could be isolated as the only erbium-containing product in a yield of 77%. To aid structural characterization in solution, the isostructural yttrium complexes $\mathbf{1}_{\text{Y}}$ and $\mathbf{2}_{\text{Y}}$ were also synthesized in yields of 72 and 5%, respectively, using the longer reaction time. Separation

of the two compounds was confirmed by ^1H , $^{13}\text{C}\{^1\text{H}\}$ (Figures S1–S8) and $^{29}\text{Si}\{^1\text{H}\}$ NMR spectroscopy in THF- D_8 , with ^{29}Si resonances for $\mathbf{1}_{\text{Er}}$ observed at $\delta = 12.48$ ppm for the spiro silicon and -12.09 ppm for the trimethylsilyl group (Figure S4). The analogous environments in $\mathbf{2}_{\text{Y}}$ occur at 37.29 and -16.37 ppm, respectively, in THF- D_8 (Figure S8). Using the shorter reaction time allowed $\mathbf{1}_{\text{Y}}$ to be isolated as the sole product in 82% yield.

The solid-state structures of $\mathbf{1}_{\text{Er}}$ and $\mathbf{1}_{\text{Y}}$ were determined by X-ray crystallography and found to be similar, hence only $\mathbf{1}_{\text{Er}}$ is described in detail. Consistent with their similar crystal structures, the two compounds also have very similar FTIR spectra (Figure S9). Structural parameters for $\mathbf{1}_{\text{Y}}$ are provided in the Supporting Information (Figure 1, Figure S17, Tables S1–S4). The structure of $\mathbf{1}_{\text{Er}}$ consists of polymeric chains with an $\eta^4\text{-L}^1$ ligand bridging through four carbon atoms between erbium and potassium. The spiro-silicon atom Si3 is tetrahedral and, hence, not coordinated to either metal. The Er–C and K–C distances to L^1 are in the range



Scheme 1. Synthesis of $[(\mu\text{-}\eta^8\text{:}\eta^8\text{-COT})\text{Er}(\mu\text{-L}^1)\text{K}]_\infty$ ($\mathbf{1}_{\text{M}}$), $[(\mu\text{-}\eta^8\text{:}\eta^8\text{-COT})\text{Er}(\mu\text{-L}^1)\text{K}(\text{THF})_2]_2$ ($\mathbf{2}_{\text{M}}$) and $[(\mu\text{-}\eta^8\text{:}\eta^8\text{-COT})\text{Er}\{\mu\text{-}\eta^5\text{:}\eta^5\text{-GeC}_4\text{-}(\text{SiMe}_3)_2\text{Me}_2\}\text{K}(\text{THF})_2]_2$ ($\mathbf{3}_{\text{M}}$). $\text{M} = \text{Er}$ or Y , $\text{E} = \text{Si}$ or Ge , $\text{R}' = \text{SiMe}_3$, and $\text{R} = \text{Me}$ or Ph .

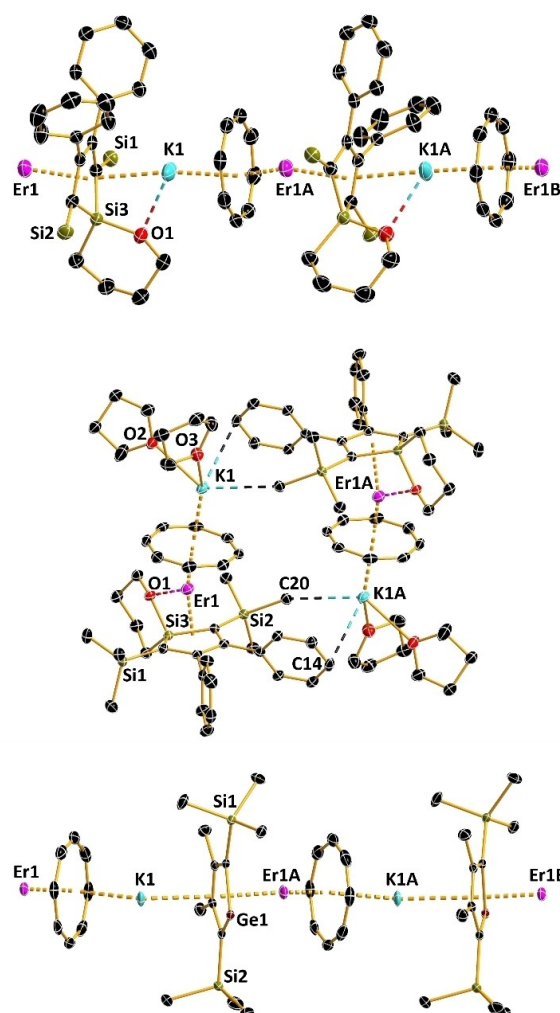


Figure 1. Thermal ellipsoid representation (50% probability) of a segment of the polymer chain of $\mathbf{1}_{\text{Er}}$ (upper), the dimeric structure of $\mathbf{2}_{\text{Er}}$ (middle) and a segment of the polymer chain of $\mathbf{3}_{\text{Er}}$ (lower). Unlabeled black atoms are carbon. For clarity, hydrogen atoms are not shown.

2.525(3)–2.570(3) Å and 3.016(3)–3.508(3) Å, respectively, and the six-membered silapyran ring coordinates through oxygen to potassium, with a K–O distance of 2.587(2) Å. The structural parameters reported by Müller et al. for the THF solvate of $[K_2Cp^{Si}]$ include C–C bond lengths in the narrow range 1.423(16)–1.438(17) Å, indicating delocalization of the π -electrons around the planar SiC_4 ring.^[39] In contrast, the C1–C2, C2–C3 and C3–C4 bond lengths in 1_{Er} alternate as 1.474(4), 1.413(4) and 1.481(4) Å, respectively. Combined with the non-planar SiC_4 ring, these data are consistent with a loss of aromaticity upon insertion of the silole into THF. The metal atoms are also bridged by an η^8 -COT ligand with Er–C and K–C distances in the range 2.530(4)–2.580(3) and 3.023(4)–3.178(3) Å.

Molecules of 2_{Er} and 2_Y are also isostructural, crystallizing as centrosymmetric dimers involving cation- π interactions between potassium and a phenyl ring (via C14), and a K...HC close contact with a trimethylsilyl substituent (via C20), reminiscent of an anagostic interaction (Figure 1, Figure S18, Tables S1, S2, S5, S6). Unlike with 1_{Er} , the activated ligand L^1 in 2_{Er} coordinates to erbium via the oxygen atom, with an Er–O distance of 2.4034(12) Å. The Er–C distances to the η^4 - L^1 and η^8 -COT ligands are in the range 2.5480(18)–2.6579 (18) Å and 2.5827(19)–2.640(2) Å, respectively. In addition, the coordination environment of potassium consists of an η^8 -COT ligand, with K–C distance in the range 3.090(2)–3.248(2) Å, and two THF ligands.

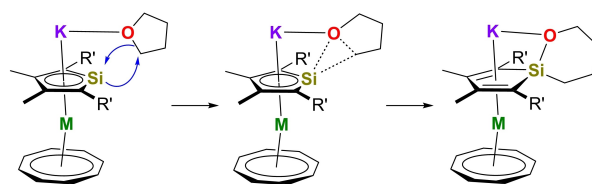
The reactions of $[K_2Cp^{Ge}]$ with $[M(\eta^8-COT)(THF)_4][BPh_4]$ ($M=Er, Y$) gave the coordination polymers $[[\eta^5-GeC_4(SiMe_3)_2Me_2]M(\eta^8-COT)K]_{\infty}$ (3_M) as the only yttrium- and erbium-containing products. The structures of 3_M (Figure 1, Figures S19, S20, Tables S1, S2, S7, S8) consist of $[[\eta^5-GeC_4(SiMe_3)_2Me_2]M(\eta^8-COT)]^-$ sandwich complexes bridged by potassium cations, with the germole ligands remaining intact. In 3_{Er} , the Er–C and Er–Ge distance to the η^5 -germole ligand are 2.568(4)–2.603(4) and 2.8863(5) Å, respectively, and the analogous distances to potassium are 3.091(4)–3.207(4) and 3.2979(9) Å, respectively. The C1–C2, C2–C3 and C3–C4 distances in 3_{Er} are 1.428(6), 1.421(6) and 1.435(6) Å, respectively, indicating π -electron delocalization around the germole ring, which is consistent with its planarity and the sum of the internal angles being 540° .^[39] The Er–C and K–C distances to the η^8 -COT ligand are 2.507(5)–2.564(5) Å and 3.067(4)–3.351(4), respectively. Inter-chain interactions are also present in the structure of 3_{Er} owing to the germanium-centered electron lone pair engaging in dative interactions with potassium, resulting in a Ge–K distance of 3.5640(10) Å. The same pattern of bond lengths occurs in the structure of 3_Y . The 1H and ^{13}C - $\{^1H\}$ NMR spectroscopy data for 3_Y in solution are also consistent with the solid-state structure (Figures S12–S14), including a single resonance in the $^{29}Si\{^1H\}$ NMR spectrum at $\delta = -13.65$ ppm (Figure S15).

The sensitivity of THF to polar main group organometallics, especially organolithium reagents, is well-known and often results in cleavage of the ring to give a metal enolate and ethene.^[40,41] Other ring-opening reactions of THF include activation by frustrated Lewis pairs^[42] and heterobimetallic main group reagents.^[43] Selective deprotonation of THF without ring opening by sodium zincate reagents and subsequent functionalization have also been described.^[44] Ring expansion of THF is, however, rare, having been observed previously in a handful of instances with aluminium(I) reagents.^[45,46] To the best of our knowledge, the formation of 1_M and 2_M are the first examples of silicon inserting into the THF ring, formally representing a silicon(II)-silicon(IV) oxidative addition. Notably, 1H NMR spectroscopy reveals that when $[K_2Cp^{Si}]$ alone is subjected to prolonged heating under reflux, silole insertion into THF- D_8 does not occur (Figure S11). Hence, formation of 1_M and 2_M requires potassium and the rare earth metal to be present, providing an example of mixed-metal synergic reactivity. Since THF activation is not observed in the analogous reactions of $[K_2Cp^{Ge}]$ with $[Er(\eta^8-COT)(THF)_4][BPh_4]$ to give 3_M , the stronger nucleophilicity of the silole presumably plays an important role. A mechanism to account for the formation of 1_M can therefore be proposed in which THF coordination to potassium brings the substrate into proximity with the nucleophilic silicon atom, which then attacks the 2-position (Scheme 2). An alternative mechanism with initial coordination of THF to the rare-earth metal is also conceivable, leading to formation of 2_M .

Erbium complexes consisting of the $\{Er(\eta^8-COT)\}^+$ building block are well-known for their slow magnetic relaxation properties, which is thought to arise from complementarity between the prolate spheroidal electron density of Er^{3+} and the equatorial crystal field provided by $[COT]^{2-}$.^[47,48] It is, therefore, of interest to determine the impact of silole insertion on the crystal field experienced by erbium in 1_{Er} and 2_{Er} , and to compare this to the properties of the intact germole-ligated complex 3_{Er} .

Firstly, the molar magnetic susceptibility of the three compounds was measured in an applied field of 1 kOe and found to be characteristic of Er^{3+} , with $\chi_M T$ reaching 11.16, 11.51 and 11.53 $cm^3 K mol^{-1}$ at 300 K for 1_{Er} , 2_{Er} and 3_{Er} , respectively, close to the theoretical value of 11.48 $cm^3 K mol^{-1}$ for an isolated Er^{3+} ion ($^4I_{15/2}$ ground state) (Figures S21–S23).^[49] At 2 K, the magnetization for each compound increases rapidly as the DC field increases to about 15 kOe before increasing more gradually at higher fields, and approaching saturation at 70 kOe, reaching 5.00, 5.06 and 4.98 $N\beta$ in 1_{Er} , 2_{Er} and 3_{Er} , respectively (Figures S21–S23). The occurrence of magnetic blocking in 1_{Er} and 3_{Er} was indicated by bifurcations in the field-cooled/zero-field-cooled (FC/ZFC) magnetic susceptibility as a function of temperature at 2.5 K, using an applied field of 1 kOe (Figures S24, S26). A less pronounced FC/ZFC bifurcation

was observed for 2_{Er} . The occurrence of magnetic blocking in 1_{Er} and 3_{Er} was indicated by bifurcations in the field-cooled/zero-field-cooled (FC/ZFC) magnetic susceptibility as a function of temperature at 2.5 K, using an applied field of 1 kOe (Figures S24, S26). A less pronounced FC/ZFC bifurcation



Scheme 2. Possible mechanism to account for silole insertion into THF, leading to formation of 1_M ($M=Er$ or Y).

was observed for $\mathbf{2}_{\text{Er}}$ at 2 K (Figure S25). Broadly consistent with these observations, magnetic hysteresis measurements revealed slightly open, S-shaped loops at 2 K for all three compounds, which close at higher temperatures (Figures S27–S29).

Using a Magnetic Property Measurement System (MPMS), the real and imaginary components of the AC susceptibility were determined as functions of frequency and of temperature, i.e., $\chi'(\nu)$, $\chi''(\nu)$, $\chi'(T)$ and $\chi''(T)$, in zero DC field, an AC field of 3 Oe, and frequencies up to 941 Hz. SMM behaviour was observed for all three compounds (Figure 2, Figures S30, S31, S35, S36, S40, S41). For $\mathbf{1}_{\text{Er}}$, the maxima in $\chi''(\nu)$ are almost temperature independent in the region 2–4.5 K, before shifting to higher frequencies as the temperature increases to 14.5 K. Above 14.5 K, maxima were not observed in the standard frequency range. From these data, Cole-Cole plots of $\chi''(\chi')$ were produced and fitted, allowing relaxation times (τ) to be extracted (Figure S32, Table S9). The ensuing plot of $\ln\tau$ versus T^{-1} revealed a near-linear dependence in the region 9.5–12 K followed by curvature down to 4.5 K, and almost temperature-independent relaxation down to 2 K (Figure 2, Figures S33–S34). The magnetic relaxation times for $\mathbf{1}_{\text{Er}}$ show the hallmarks of an SMM in which the high-temperature relaxation is dominated by Orbach relaxation, whereas quantum tunneling of the magnetization (QTM) is dominant at lower temperatures, with Raman processes occurring at intermediate temperatures. A fit of the relaxation times was obtained using $\tau^{-1} = \tau_0^{-1} e^{-U_{\text{eff}}/k_{\text{B}}T} + CT^n + \tau_{\text{QTM}}^{-1}$, where the attempt rate is τ_0^{-1} , U_{eff} is the effective energy barrier, C and n denote the Raman coefficient and Raman exponent, respectively, and the rate of QTM is τ_{QTM}^{-1} . For $\mathbf{1}_{\text{Er}}$, the parameters obtained from this analysis are $\tau_0 = 1.09 \times 10^{-9}$ s,

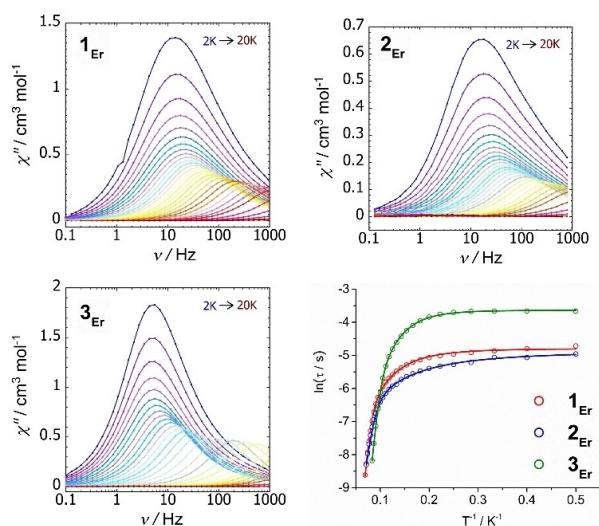


Figure 2. Plots of $\chi''(\nu)$ data for $\mathbf{1}_{\text{Er}}$ (top left), $\mathbf{2}_{\text{Er}}$ (top right) and $\mathbf{3}_{\text{Er}}$ (bottom left) in zero DC field; solid lines are a guide for the eye. Temperature dependence of the relaxation time for all three compounds; solid lines represent fits to the data using the parameters stated in the text.

$U_{\text{eff}} = 122 \pm 4 \text{ cm}^{-1}$, $C = 0.20 \pm 0.05 \text{ s}^{-1} \text{ K}^{-n}$, $n = 3.18 \pm 0.1$, and $\tau_{\text{QTM}} = 9.1 \pm 0.15 \text{ ms}$ (Table 1).

The AC susceptibility properties and relaxation times determined for $\mathbf{2}_{\text{Er}}$ and $\mathbf{3}_{\text{Er}}$ are similar to those of $\mathbf{1}_{\text{Er}}$, with $\mathbf{2}_{\text{Er}}$ displaying $\chi''(\nu)$ and $\chi''(T)$ maxima at temperatures in the range 2–14 K and $\mathbf{3}_{\text{Er}}$ in the range 2–15 K (Figure 2, Figures S35–S36, S40, S41). The parameters extracted from fits of $\ln\tau$ versus T^{-1} for $\mathbf{2}_{\text{Er}}$ are $\tau_0 = 8.51 \times 10^{-8}$ s, $U_{\text{eff}} = 80 \pm 1.5 \text{ cm}^{-1}$, $C = 1.95 \pm 0.5 \times \text{s}^{-1} \text{ K}^{-n}$, $n = 2.31 \pm 0.11$, and $\tau_{\text{QTM}} = 7.2 \pm 0.22 \text{ ms}$ (Figures S37–S39, Table 1, Table S10), and for $\mathbf{3}_{\text{Er}}$ they are $\tau_0 = 5.52 \times 10^{-9}$ s, $U_{\text{eff}} = 91 \pm 3.5 \text{ cm}^{-1}$, $C = 0.04 \pm 0.01 \text{ s}^{-1} \text{ K}^{-n}$, $n = 3.55 \pm 0.36$, and $\tau_{\text{QTM}} = 28 \pm 2.2 \text{ ms}$ (Figures S42–S44, Table 1, Table S11).

For SMMs based on erbium-COT units, such as $[\text{Er}(\eta^8\text{-COT}^{\text{R}})_2]^-$ ($\text{COT}^{\text{R}} = \text{C}_8\text{H}_8$, 1,4- $\text{C}_8\text{H}_6(\text{SiMe}_3)_2$), $[(\eta^5\text{-Cp}^{\text{R}})\text{Er}(\eta^8\text{-COT}^{\text{R}})_2]$ ($\text{Cp}^{\text{R}} = \text{C}_5\text{Me}_5$, $\text{C}_5\text{Bu}_3\text{H}_2$, phospholy), and $[(\eta^8\text{-COT})\text{ErXL}_{x/y}]$ ($\text{X} = \text{Cl}$, I ; $\text{L} = \text{THF}$, pyridine, MeCN, ; $x = 1$, $y = 2$; $x = 2$, $y = 1$), U_{eff} values are typically in the range 10–250 cm^{-1} , with the larger barriers occurring in the absence of a strong, competing axial crystal field.^[47,48,50–57] The energy barriers determined for $\mathbf{1}_{\text{Er}}$ – $\mathbf{3}_{\text{Er}}$ using a standard AC susceptometry are therefore consistent with literature precedent. The larger barrier(s) determined for $\mathbf{1}_{\text{Er}}$ can be rationalized in terms of the relatively short Er–COT centroid distance of 1.77599(19) Å, which enhances the equatorial component of the crystal field, and the relatively long Er–L¹ centroid distance of 2.27656(19) Å, which diminishes the axial component. The analogous Er–COT and Er–L¹ distances in $\mathbf{2}_{\text{Er}}$ are 1.85829(15) and 2.27195(15) Å, hence the equatorial crystal field should be less dominant and the barrier smaller, as observed. In $\mathbf{3}_{\text{Er}}$ the Er–COT and Er–Cp^{Gc} distances are 1.74178(19) and 2.24837(19) Å, respectively, hence a comparable equatorial crystal field to $\mathbf{1}_{\text{Er}}$ but a relatively strong axial crystal field, leading to a smaller barrier.

A common feature in the AC susceptibility responses of erbium-COT SMMs is that both χ' and χ'' clearly continue their frequency dependence well beyond the upper limit of the commercial instrument, i.e., typically 1–1.5 or 10 kHz for an MPMS or Physical Property Measurement System (PPMS), respectively. Noting that AC susceptibility studies of molecular magnets have been reported at frequencies in the region of 70–95 kHz,^[58,59] if the frequency window could be extended further, deeper insight into the magnetization dynamics in the activated relaxation regime at higher temperatures would be obtained. Compound $\mathbf{1}_{\text{Er}}$ was therefore selected for high-frequency (HF) AC susceptibility

Table 1: SMM relaxation parameters for $\mathbf{1}_{\text{Er}}$, $\mathbf{2}_{\text{Er}}$ and $\mathbf{3}_{\text{Er}}$.

	$\mathbf{1}_{\text{Er}}$	$\mathbf{1}_{\text{Er}}^{\text{[a]}}$	$\mathbf{2}_{\text{Er}}$	$\mathbf{3}_{\text{Er}}$
τ_0/s	1.09×10^{-9}	3.76×10^{-11}	8.51×10^{-8}	5.52×10^{-9}
$U_{\text{eff}}/\text{cm}^{-1}$	122 ± 4	156 ± 1.5	80 ± 1.5	91 ± 3.5
$C/\text{s}^{-1} \text{ K}^{-n}$	0.2 ± 0.05	0.05 ± 0.02	1.95 ± 0.5	0.04 ± 0.01
n	3.18 ± 0.1	3.82 ± 0.19	2.31 ± 0.11	3.55 ± 0.36
$\tau_{\text{QTM}}/\text{ms}$	9.1 ± 0.15	7.88 ± 0.26	7.2 ± 0.22	28 ± 2.2

[a] Determined with inclusion of high-frequency susceptibility measurements.

measurements, which were performed on a bespoke AC susceptometer installed within a PPMS and operating at frequencies from 10 kHz up to 10³ kHz, going beyond the MPMS frequency window by three orders of magnitude. The details of this instrument have been described previously by Riordan et al.^[60]

Using an AC field of 1 Oe, the HF measurements on **1_{Er}** revealed additional maxima in $\chi''(\nu)$ up to 25 K (Figure 3, Figure S45). The noise in the HF data is a consequence of the dielectric background associated with the unsymmetrical shape of the flame-sealed NMR tube sample container. Cole-Cole plots of $\chi''(\chi')$ from 15–25 K are parabolic and were fitted using the same method as for the lower-frequency measurements (Figures S46–S47, Table S12), allowing relaxation times to be extracted and merged with those corresponding to the lower-frequency data. A revised plot of $\ln\tau$ versus T^{-1} for **1_{Er}** shows that the linear dependence of the relaxation time and, therefore, the Orbach relaxation continue up to 25 K. The resulting fit parameters for the frequency range 0.1 Hz to 10³ kHz are $\tau_0 = 3.76 \times 10^{-11}$ s, $U_{\text{eff}} = 156 \pm 1.5$ cm⁻¹, $C = 0.05 \pm 0.02$ s⁻¹ K⁻ⁿ, $n = 3.82 \pm 0.19$, and $\tau_{\text{QTM}} = 7.88 \pm 0.26$ ms. A noteworthy outcome from the HF susceptibility measurements is the increase in the energy barrier from 122 to 156 cm⁻¹, with the latter being a more reliable owing to the inclusion of more

data points over a wider temperature range. This result may have implications for the determination of U_{eff} values within the conventional frequency windows of AC susceptometry, particularly when few data points and a narrow temperature range are included in the fitting process.

To delve deeper into the electronic structure of **1_{Er}**, **2_{Er}** and **3_{Er}**, multireference ab initio calculations of the CASSCF/QDPT/SINGLE_ANISO type were carried out on computationally tractable fragments of the crystal structures using the ORCA 5.0.2 software package.^[61,62] For **1_{Er}**, the selected fragment is $[(\eta^8\text{-COT})\text{Er}(\mu\text{-L}^1)\text{K}]$ (**1_{Er}**), for **2_{Er}** the fragment is $[(\eta^8\text{-COT})\text{Er}(\mu\text{-L}^1)\text{K}(\text{THF})]$ (**2_{Er}**), and for **3_{Er}** the fragment is $[(\eta^5\text{-GeC}_4(\text{SiMe}_3)_2\text{Me}_2)\text{M}(\eta^8\text{-COT})]^-$ (**3_{Er}**) (Figure 4).

The effect of the crystal field on the ⁴I_{15/2} ground state of Er³⁺ in **1_{Er}**, **2_{Er}** and **3_{Er}** is to split the eight Kramers doublets (KDs) across energies of 293, 384 and 259 cm⁻¹, respectively (Table S13). In the ground KDs of **1_{Er}** and **3_{Er}**, the axial symmetry of the crystal field is reflected in the *g*-tensors, which are calculated to be $g_x = 0.004$, $g_y = 0.006$ and $g_z = 17.29$, and $g_x = 0.002$, $g_y = 0.004$ and $g_z = 17.75$, respectively (Tables S14, S16). The analogous parameters for **2_{Er}** are $g_x = 0.091$, $g_y = 0.136$ and $g_z = 16.831$ (Table S15), with

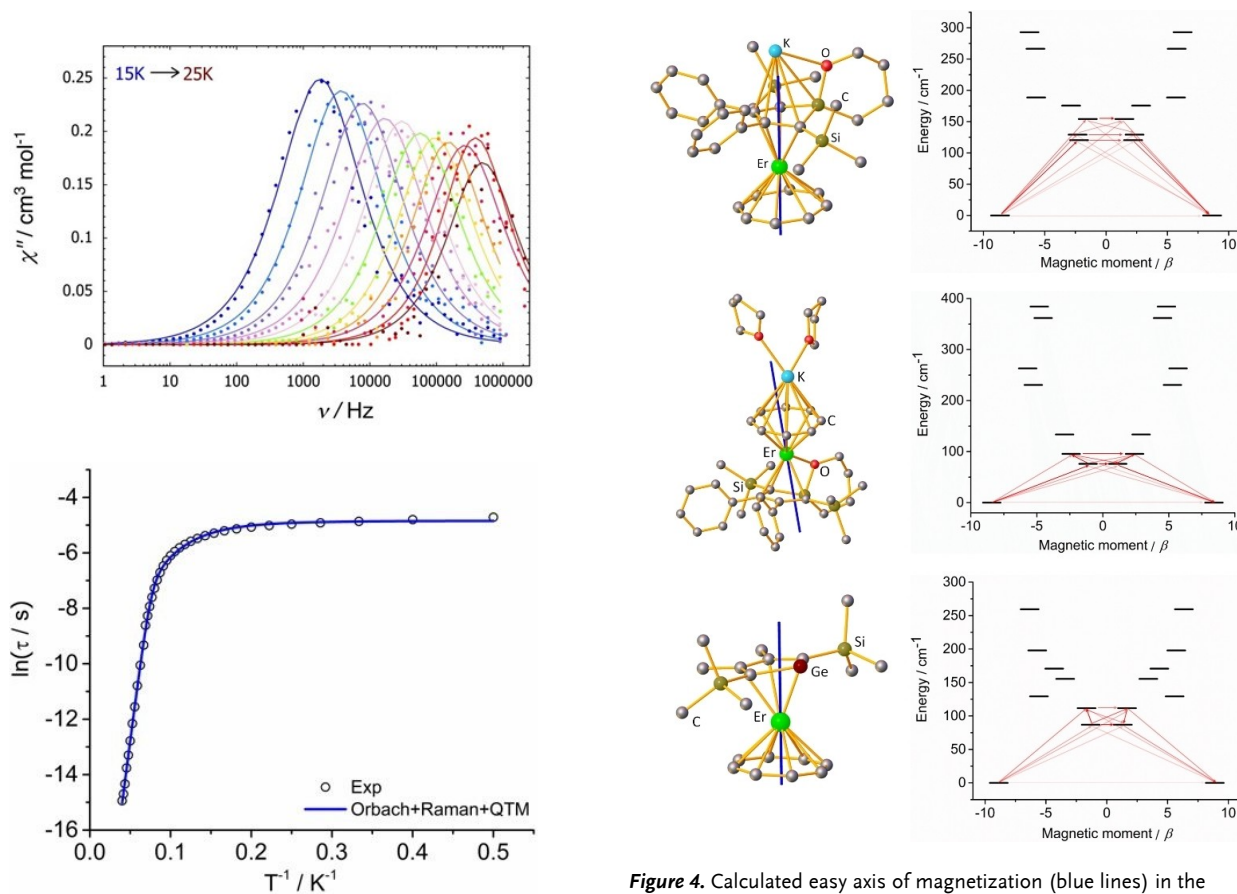


Figure 3. High-frequency $\chi''(\nu)$ data for **1_{Er}** (top), and temperature dependence of the relaxation time in the temperature range 2–25 K (bottom). Solid lines represent fits to the data using the parameters stated in the text.

Figure 4. Calculated easy axis of magnetization (blue lines) in the ground KD and magnetic relaxation barriers for **1_{Er}** (top), **2_{Er}** (middle) and **3_{Er}** (bottom). Red lines represent transition magnetic moments, with stronger shading indicating a more probable transition. For clarity, hydrogen atoms are not shown, and transitions involving higher-energy states not involved in the relaxation mechanism are omitted.

the greater transverse components presumably a consequence of the Er–O interaction with the equatorial silapyran ring. The wavefunction compositions of the ground KDs for $\mathbf{1}'_{\text{Er}}$ and $\mathbf{3}'_{\text{Er}}$ consist of 91 % and 97 % $|M_J| = 15/2$ character (Tables S14, S16), respectively, with the easy axis of magnetization passing almost through the centres of the η^n -ligands (Figure 4). In contrast, the ground KD for $\mathbf{2}'_{\text{Er}}$ consist of only 84 % $|M_J| = 15/2$ character, with non-negligible mixing of higher-lying KDs into the ground KD (Table S15) and the easy axis of magnetization oriented towards the edges of the two η^n -ligands (Figure 4). The first-excited KDs in $\mathbf{1}'_{\text{Er}}$, $\mathbf{2}'_{\text{Er}}$ and $\mathbf{3}'_{\text{Er}}$ lie at energies of 120, 76 and 87 cm^{-1} , respectively, with all three showing greatly diminished axial character owing to extensive mixing of M_J wavefunctions (Tables S14–S16). The calculated transition magnetic moment matrix elements for barrier crossing within the first-excited KD are also appreciable (Tables S17–S19). Considering the good match between experimental and calculated effective energy barriers, Orbach relaxation in all three SMMs should, therefore, proceed via the first-excited KD, as shown in Figure 4.

Returning to the question of how the group 14 heteroatom within the dianionic metallole ligand impacts on the SMM properties, compounds $\mathbf{1}_{\text{Er}}$ and $\mathbf{3}_{\text{Er}}$ and their simplified fragments $\mathbf{1}'_{\text{Er}}$ and $\mathbf{3}'_{\text{Er}}$ allow the most meaningful comparison since neither feature equatorial coordination at the erbium centres. Key relaxation parameters determined through bulk magnetic measurements differ for $\mathbf{1}_{\text{Er}}$ and $\mathbf{3}_{\text{Er}}$, yet their U_{eff} values are similar, and both are comparable to the barriers determined for other erbium-COT SMMs. Furthermore, although the calculated properties of $\mathbf{1}'_{\text{Er}}$ and $\mathbf{3}'_{\text{Er}}$, such as g -tensors and crystal field parameters, are quantitatively different (Tables S14, S16, S20), they are clearly similar overall. Therefore, despite the activation of $[\text{Cp}^{\text{Si}}]^{2-}$ to give $[\text{L}^1]^{2-}$ in the synthesis of $\mathbf{1}_{\text{Er}}$, as opposed to intact transfer of $[\text{Cp}^{\text{Ge}}]^{2-}$ when forming $\mathbf{3}_{\text{Er}}$, the overall impact on the dynamic magnetic properties is not appreciable. This observation points towards the formal dianionic charge of the axial $[\text{L}^1]^{2-}$ and $[\text{Cp}^{\text{Ge}}]^{2-}$ ligands playing a dominant role in the crystal field, rather than a heteroatom-specific effect, at least for the compounds considered in this study.

Conclusion

In conclusion, mixed-metal synergy arising from reactions of the potassium silole $[\text{K}_2\text{Cp}^{\text{Si}}]$ with the yttrium and erbium half-sandwich compounds $[\text{M}(\eta^8\text{-COT})(\text{THF})_4][\text{BPh}_4]$ results in the η^5 -silole ligand inserting the nucleophilic silicon centre into a C–O bond of THF. The resulting sandwich complexes $\mathbf{1}_{\text{M}}$ and $\mathbf{2}_{\text{M}}$ contain an unusual spiro-bicyclic silapyran ring formed by formal oxidative addition across silicon(II) to give silicon(IV), with coordination of the pyran oxygen atom to potassium in $\mathbf{1}_{\text{M}}$ or to the rare-earth metal in product $\mathbf{2}_{\text{M}}$. In contrast, the analogous reactions involving the η^5 -germole ligand $[\text{Cp}^{\text{Ge}}]^{2-}$ proceed with intact germole transfer to the rare-earth metal, forming $\mathbf{3}_{\text{M}}$. The erbium derivatives are SMMs, with energy barriers of 122, 80 and

91 cm^{-1} for $\mathbf{1}_{\text{Er}}$, $\mathbf{2}_{\text{Er}}$ and $\mathbf{3}_{\text{Er}}$, respectively. High-frequency AC susceptometry revealed that Orbach relaxation in $\mathbf{1}_{\text{Er}}$ is dominant up to at least 25 K. A magneto-structural correlation revealed similarities between the electronic structure of $\mathbf{1}_{\text{Er}}$ and $\mathbf{3}_{\text{Er}}$. The presence of different heteroatoms in the metallole ligands does not impact significantly on the SMM properties. Instead, the relatively short distance from erbium to the centroid of the dianionic germole ligand in $\mathbf{3}_{\text{Er}}$ is likely to be responsible for the lower barrier compared to $\mathbf{1}_{\text{Er}}$.

Supporting Information

The authors have cited additional references within the Supporting Information.[63–74] Crystallography data in CIF format have been deposited at the Cambridge Crystallographic Data Centre with reference codes 2285167 ($\mathbf{1}_{\text{Er}}\cdot\text{THF}$), 2285169 ($\mathbf{2}_{\text{Er}}$), 2285168 ($\mathbf{3}_{\text{Er}}$), 2285171 ($\mathbf{1}_{\text{Y}}\cdot\text{THF}$), 2285172 ($\mathbf{2}_{\text{Y}}$), and 2285173 ($\mathbf{3}_{\text{Y}}$). Other data that support the findings of this study are openly available at DOI: 10.25377/sussex.25119179.

Acknowledgements

The authors thank the EPSRC for financial support (grants EP/V003089/1, EP/V046659/1 and EP/X036626/1), and Prof. T. Lancaster and Dr. M. J. Raine (University of Durham) for providing magnetic data on the erbium compounds (MPMS funded by EPSRC grant EP/V054031/1).

Conflict of Interest

The authors declare no conflict of interest.

Data Availability Statement

The data that support the findings of this study are openly available in Figshare at <https://doi.10.25377/sussex.25119179>, reference number 0.

Keywords: silicon · rare earths · mixed-metal synergy · potassium · magnetic properties

- [1] N. Ishikawa, M. Sugita, T. Ishikawa, S. Y. Koshihara, Y. Kaizu, *J. Am. Chem. Soc.* **2003**, *125*, 8694–8695.
- [2] D. N. Woodruff, R. E. P. Winpenny, R. A. Layfield, *Chem. Rev.* **2013**, *113*, 5110–5148.
- [3] K. Bernot, *Eur. J. Inorg. Chem.* **2023**, e202300336.
- [4] M. Atzori, R. Sessoli, *J. Am. Chem. Soc.* **2019**, *141*, 11339–11352.
- [5] E. Moreno-Pineda, W. Wernsdorfer, *Nat. Rev. Phys.* **2021**, *3*, 645–659.
- [6] S. Mondal, A. Lunghi, *J. Am. Chem. Soc.* **2022**, *144*, 22965–22975.

- [7] M. Briganti, F. Santanni, L. Tesi, F. Totti, R. Sessoli, A. Lunghi, *J. Am. Chem. Soc.* **2021**, *143*, 13633–13645.
- [8] D. Reta, J. G. C. Kragoskow, N. F. Chilton, *J. Am. Chem. Soc.* **2021**, *143*, 5943–5950.
- [9] A. Lunghi, F. Totti, S. Sanvito, R. Sessoli, *Chem. Sci.* **2017**, *8*, 6051–6059.
- [10] A. Lunghi, F. Totti, R. Sessoli, S. Sanvito, *Nat. Commun.* **2017**, *8*, 14620.
- [11] J.-L. Liu, Y.-C. Chen, Y.-Z. Zheng, W.-Q. Lin, L. Ungur, W. Wernsdorfer, L. F. Chibotaru, M.-L. Tong, *Chem. Sci.* **2013**, *4*, 3310–3316.
- [12] Z.-H. Li, Y.-Q. Zhai, W.-P. Chen, Y.-S. Ding, Y.-Z. Zheng, *Chem. Eur. J.* **2019**, *25*, 16219–16224.
- [13] Y.-S. Ding, N. F. Chilton, R. E. P. Winpenny, Y.-Z. Zheng, *Angew. Chem. Int. Ed.* **2016**, *55*, 16071–16074.
- [14] A. B. Canaj, S. Dey, E. R. Martí, C. Wilson, G. Rajaraman, M. Murrie, *Angew. Chem. Int. Ed.* **2019**, *58*, 14146–14151.
- [15] S. Demir, M. I. Gonzalez, L. E. Darago, W. J. Evans, J. R. Long, *Nat. Commun.* **2017**, *8*, 2144.
- [16] P. Zhang, Q.-C. Luo, Z. Zhu, W. He, N. Song, J. Lv, X. Wang, Q.-G. Zhai, Y.-Z. Zheng, J. Tang, *Angew. Chem. Int. Ed.* **2023**, *62*, e202218540.
- [17] N. Mavragani, D. Errulat, D. A. Gálico, A. A. Kitos, A. Mansikkamäki, M. Murugesu, *Angew. Chem. Int. Ed.* **2021**, *60*, 24206–24213.
- [18] F. Liu, L. Spree, D. S. Krylov, G. Velkos, S. M. Avdoshenko, A. A. Popov, *Acc. Chem. Res.* **2019**, *52*, 2981–2993.
- [19] F. Liu, D. S. Krylov, L. Spree, S. M. Avdoshenko, N. A. Samoylova, M. Rosenkranz, A. Kostanyan, T. Greber, A. U. B. Wolter, B. Büchner, A. A. Popov, *Nat. Commun.* **2017**, *8*, 16098.
- [20] G. Velkos, D. S. Krylov, K. Kirkpatrick, L. Spree, V. Dubrovin, B. Büchner, S. M. Avdoshenko, V. Bezmelnitsyn, S. Davis, P. Faust, J. Duchamp, H. C. Dorn, A. A. Popov, *Angew. Chem. Int. Ed.* **2019**, *58*, 5891–5896.
- [21] F.-S. Guo, B. M. Day, Y.-C. Chen, M.-L. Tong, A. Mansikkamäki, R. A. Layfield, *Angew. Chem. Int. Ed.* **2017**, *56*, 11145–11149.
- [22] C. A. P. Goodwin, F. Ortu, D. Reta, N. F. Chilton, D. P. Mills, *Nature* **2017**, *548*, 439.
- [23] K. Randall McClain, C. A. Gould, K. Chakarawat, S. J. Teat, T. J. Groshens, J. R. Long, B. G. Harvey, *Chem. Sci.* **2018**, *9*, 8492–8503.
- [24] C. G. T. Price, A. Mondal, J. P. Durrant, J. Tang, R. A. Layfield, *Inorg. Chem.* **2023**, *62*, 9924–9933.
- [25] M. He, F.-S. Guo, J. Tang, A. Mansikkamäki, R. A. Layfield, *Chem. Sci.* **2020**, *11*, 5745–5752.
- [26] M. He, F.-S. Guo, J. Tang, A. Mansikkamäki, R. A. Layfield, *Chem. Commun.* **2021**, 6396, 6396.
- [27] D. Errulat, B. Gabidullin, A. Mansikkamäki, M. Murugesu, *Chem. Commun.* **2020**, 56, 5937–5940.
- [28] A. H. Vincent, Y. L. Whyatt, N. F. Chilton, J. R. Long, *J. Am. Chem. Soc.* **2023**, *145*, 1572–1579.
- [29] S. De, A. Mondal, Z.-Y. Ruan, M.-L. Tong, R. A. Layfield, *Chem. Eur. J.* **2023**, *29*, e202300567.
- [30] L. Münzfeld, X. Sun, S. Schlittenhardt, C. Schoo, A. Hauser, S. Gillhuber, F. Weigend, M. Ruben, P. W. Roesky, *Chem. Sci.* **2022**, *13*, 945–954.
- [31] F.-S. Guo, M. He, G.-Z. Huang, S. R. Giblin, D. Billington, F. W. Heinemann, M.-L. Tong, A. Mansikkamäki, R. A. Layfield, *Inorg. Chem.* **2022**, *61*, 6017–6025.
- [32] P. Evans, D. Reta, G. F. S. Whitehead, N. F. Chilton, D. P. Mills, *J. Am. Chem. Soc.* **2019**, *141*, 19935–19940.
- [33] J. C. Vanjak, B. O. Wilkins, V. Vieru, N. S. Bhuvanesh, J. H. Reibenspies, C. D. Martin, L. F. Chibotaru, M. Nippe, *J. Am. Chem. Soc.* **2022**, *144*, 17743–17747.
- [34] X. Sun, L. Münzfeld, D. Jin, A. Hauser, P. W. Roesky, *Chem. Commun.* **2022**, 58, 7976–7979.
- [35] M. Saito, *Acc. Chem. Res.* **2018**, *51*, 160–169.
- [36] W. P. Freeman, T. D. Tilley, A. L. Rheingold, *J. Am. Chem. Soc.* **1994**, *116*, 8428–8429.
- [37] W. P. Freeman, T. D. Tilley, L. M. Liable-Sands, A. L. Rheingold, *J. Am. Chem. Soc.* **1996**, *118*, 10457–10468.
- [38] Z. Dong, C. R. W. Reinhold, M. Schmidtman, T. Müller, *J. Am. Chem. Soc.* **2017**, *139*, 7117–7123.
- [39] Z. Dong, C. R. W. Reinhold, M. Schmidtman, T. Müller, *Organometallics* **2018**, *37*, 4736–4743.
- [40] a) R. B. Bates, L. M. Kroposki, D. E. Potter, *J. Org. Chem.* **1972**, *37*, 560–562; b) M. J. Evans, A. O'Reilly, M. D. Anker, M. P. Coles, *Organometallics* **2022**, *41*, 2657–2661.
- [41] A. Maercker, *Angew. Chem. Int. Ed.* **1987**, *26*, 972–989.
- [42] A. Solovyev, E. Lacôte, D. P. Curran, *Dalton Trans.* **2013**, *42*, 695–700.
- [43] R. E. Mulvey, V. L. Blair, W. Clegg, A. R. Kennedy, J. Klett, L. Russo, *Nat. Chem.* **2010**, *2*, 588–591.
- [44] A. R. Kennedy, J. Klett, R. E. Mulvey, D. S. Wright, *Science* **2009**, *326*, 706–708.
- [45] R. J. Schwamm, M. P. Coles, M. S. Hill, M. F. Mahon, C. L. McMullin, N. A. Rajabi, A. S. S. Wilson, *Angew. Chem. Int. Ed.* **2020**, *59*, 3928–3932.
- [46] M. Schormann, K. S. Klimek, H. Hatop, S. P. Varkey, H. W. Roesky, C. Lehmann, C. Röpken, R. Herbst-Immer, M. Noltemeyer, *J. Solid State Chem.* **2001**, *162*, 225–236.
- [47] K. R. Meihaus, J. R. Long, *J. Am. Chem. Soc.* **2013**, *135*, 17952–17957.
- [48] L. Ungur, J. J. Le Roy, I. Korobkov, M. Murugesu, L. F. Chibotaru, *Angew. Chem. Int. Ed.* **2014**, *53*, 4413–4417.
- [49] C. Benelli, D. Gatteschi, in *Introduction to Molecular Magnetism*, John Wiley & Sons, Ltd, **2015**, pp. 1–23.
- [50] J. J. Le Roy, L. Ungur, I. Korobkov, L. F. Chibotaru, M. Murugesu, *J. Am. Chem. Soc.* **2014**, *136*, 8003–8010.
- [51] J. D. Hilgar, B. S. Flores, J. D. Rinehart, *Chem. Commun.* **2017**, 53, 7322–7324.
- [52] S.-M. Chen, J. Xiong, Y.-Q. Zhang, Q. Yuan, B.-W. Wang, S. Gao, *Chem. Sci.* **2018**, *9*, 7540–7545.
- [53] J. D. Hilgar, M. G. Bernbeck, J. D. Rinehart, *J. Am. Chem. Soc.* **2019**, *141*, 1913–1917.
- [54] J. J. Le Roy, I. Korobkov, M. Murugesu, *Chem. Commun.* **2014**, *50*, 1602–1604.
- [55] M. G. Bernbeck, J. D. Hilgar, J. D. Rinehart, *Polyhedron* **2020**, *175*, 114206.
- [56] J. D. Hilgar, M. G. Bernbeck, B. S. Flores, J. D. Rinehart, *Chem. Sci.* **2018**, *9*, 7204–7209.
- [57] S.-D. Jiang, B.-W. Wang, H.-L. Sun, Z.-M. Wang, S. Gao, *J. Am. Chem. Soc.* **2011**, *133*, 4730–4733.
- [58] A. Caneschi, D. Gatteschi, N. Lalioti, C. Sangregorio, R. Sessoli, G. Venturi, A. Vindigni, A. Rettori, M. G. Pini, M. A. Novak, *Angew. Chem. Int. Ed.* **2001**, *40*, 1760–1763.
- [59] G. Huang, X. Yi, F. Gendron, B. Le Guennic, T. Guizouarn, C. Daiguebonne, G. Calvez, Y. Suffren, O. Guillou, K. Bernot, *Dalton Trans.* **2019**, *48*, 16053–16061.
- [60] E. Riordan, J. Blomgren, C. Jonasson, F. Ahrentorp, C. Johansson, D. Margineda, A. Elfassi, S. Michel, F. Dell'ova, G. M. Klemencic, S. R. Giblin, *Rev. Sci. Instrum.* **2019**, *90*, 073908.
- [61] F. Neese, F. Wennmohs, U. Becker, C. Riplinger, *J. Chem. Phys.* **2020**, *152*, 224108.
- [62] F. Neese, *WIREs Comput. Mol. Sci.* **2018**, *8*, e1327.

Manuscript received: November 20, 2023

Accepted manuscript online: February 1, 2024

Version of record online: February 21, 2024